



Open Archive Toulouse Archive Ouverte

OATAO is an open access repository that collects the work of Toulouse researchers and makes it freely available over the web where possible

This is an author's version published in: <http://oatao.univ-toulouse.fr/26676>

Official URL:

<https://doi.org/10.1016/j.combustflame.2020.03.026>

To cite this version:

Dupuy, Fabien and Gatti, Marco and Mirat, Clément and Gicquel, Laurent and Nicoud, Franck and Schuller, Thierry Combining analytical models and LES data to determine the transfer function from swirled premixed flames. (2020) Combustion and Flame, 217. 222-236. ISSN 0010-2180

Any correspondence concerning this service should be sent to the repository administrator: tech-oatao@listes-diff.inp-toulouse.fr

Combining analytical models and LES data to determine the transfer function from swirled premixed flames

Fabien Dupuy^{a,b,*}, Marco Gatti^c, Clément Mirat^c, Laurent Gicquel^a, Franck Nicoud^e, Thierry Schuller^d

^aCERFACS, 42 Avenue Gaspard Coriolis 31057 Toulouse Cedex 01, France

^bSafran Aircraft Engines, Rond-point Rene Ravaud, Moissy-Cramayel 77550, France

^cLaboratoire EM2C, CNRS, CentraleSupélec, Université Paris-Saclay, 8-10 rue Joliot Curie 91192 Gif Sur Yvette cedex, France

^dInstitut de Mécanique des Fluides de Toulouse, IMFT, Université de Toulouse, CNRS, Toulouse, France

^eIMAG, Univ. Montpellier, CNRS, Montpellier, France

A B S T R A C T

A methodology is developed where the acoustic response of a swirl stabilized flame is obtained from a reduced set of simulations. Building upon previous analytical flame transfer functions, a parametrization of the flame response is first proposed, based on six independent physical parameters: a Strouhal number, the mean flame angle with respect to the main flow direction, the vortical structures convection speed, a swirl intensity parameter, a time delay between acoustic and vortical perturbations, as well as a phase shift between bulk and local velocity signals. It is then shown how these parameters can be deduced from steady and unsteady simulations. The methodology is applied to a laboratory scale premixed swirl stabilized flame exhibiting features representative of real aero-engines. In this matter, cold and reactive flow Large Eddy Simulations are first validated by comparing results with reference data from experiments. The high fidelity simulations are seen to be able to capture the flame structure and velocity profiles at different locations while forced flame dynamics for the frequency range of interest also match the experimental data. From the same analytical transfer function model, three methodologies of increasing complexity are presented for the determination of the model parameters, depending on the available data or computational resources. A first estimation of the flame acoustic response is obtained by evaluating parameters from a single stationary flame simulation in conjunction with analytical estimations for the acoustic-convective time delay. Flame dynamics and swirl related parameters can then be determined from a series of robust treatments on pulsed simulations data to improve the model accuracy. It is shown that good qualitative agreement for the flame transfer function can be obtained from a single non-forced simulation while quantitative agreement over the frequency range of interest can be obtained using additional reactive or non-reactive pulsed simulations at one single forcing frequency corresponding to a local gain minimum. The method also naturally handles different perturbation levels.

Keywords:

Flame Transfer Function
Swirling flame
Large Eddy simulation
Analytical model

1. Introduction

Increasingly stringent regulations for pollutant emissions have lead most aeronautical engine manufacturers to aim for systems using lean premixed combustion as an efficient way to reduce NOx while maintaining a good level of performance. However, lean premixed combustors have been shown to be prone to combustion instabilities where the coupling between acoustics of the combustor

and the flame can cause structural damages to the engine [1]. In parallel to these engine developments, considerable numerical efforts have been deployed and Large Eddy Simulations (LES) for instance has proven capable of capturing combustion instabilities in complex geometries [2,3]. Given the broad range of operating conditions of an aircraft engine, and its intrinsic complexity, a systematic use of high fidelity simulations is however still out of reach at the design stage. For this reason, less numerically intensive methods have been developed in the form of low order codes for thermoacoustic instabilities where acoustics and the complex flame dynamics are decoupled.

A large majority of such codes solve the Helmholtz equation in the frequency domain and take into account the flame or the

* Corresponding author at: CERFACS, 42 Avenue Gaspard Coriolis 31057 Toulouse Cedex 01, France.

E-mail addresses: fabien.dupuy@cerfacs.fr, fabien93.dupuy@orange.fr (F. Dupuy).

associated unsteady heat release response to acoustic perturbations using a Flame Transfer Function (FTF) [4] or more recently a Flame Describing Function (PDF) to also account for non-linear effects [5,6]. This approach allows to perform parametric studies, hence enabling to tackle combustion instabilities issues during the design phase [7,8]. Examples of results obtained with flow solvers using the Finite Element Method (FEM) to determine the solution of the three-dimensional Helmholtz equation within complex geometries with complex boundary conditions, including active flames and/or eventually also damping or nonlinear effects become numerous [9–14]. These methods rely on the use of the FTF/PDF and its determination is therefore of crucial importance if one wants to control or even predict thermoacoustic instabilities. Restricting the analysis to swirled flames, the determination of FTF/PDF can be made experimentally [15–17] as well as with numerical flow simulations [18–22]. Several analytical formulations based on a level set approach are also available, but only a fraction deals with swirling flames. You et al. [23] derived a FTF model based on a triple decomposition technique of the G-equation including effects of the mean, synchronized and stochastic flow variables to deal with flow rate disturbances and also changes associated to equivalence ratio perturbations. Similar approaches were used in [24,25] to examine the FTF of turbulent partially premixed flames of arbitrary shape due to equivalence ratio perturbations.

In gas turbines, flames are highly turbulent and stabilized by a swirling flow. The injector imparts a rotating motion to the fresh gases, so that combustion occurs around an inner hot gas recirculation zone that helps anchoring the flame in the vicinity of the injection system. The Swirl number, S , is generally used to characterize the rate of rotation of the flow and is defined as the ratio between the tangential and axial momentum fluxes. Neglecting pressure terms as often done in the literature, it reads:

$$S = \frac{1}{R} \frac{\int_0^R \rho u_z u_\theta r^2 dr}{\int_0^R \rho u_z^2 r dr} \quad (1)$$

where ρ is the fluid density, u_z and u_θ are respectively the axial and tangential velocity components using cylindrical coordinates, and R is a characteristic dimension, usually the outer radius of the injection device. Recent studies [15,26,27] on swirling flame dynamics indicate that their response is not only dictated by the flame itself, but also by the swirler response as evidently shown by varying the swirler to combustion chamber backplane distance or the bulk flow velocity in the injector. Palies et al. [28] therefore proposed an analytical FTF model for inverted conical flames (or V-shaped) swirled flames based on the perturbed G-equation. In this case, the swirl action is characterized by a linear relationship between the normalized axial acoustic velocity perturbation and the tangential convective velocity perturbation generated by acoustic-vorticity conversion in the swirler [15,29]. This formulation offers an interesting insight on the mechanisms driving the response of flames subject to swirl perturbations. Note that the model in [28] uses the convectively perturbed V-flame FTF from [30] as a basis and was shown to be in good agreement with experiments for the few considered cases.

The present study extends the work from Palies et al. [28] to properly represent V-shaped swirl stabilized flames. Moreover, numerical simulations are used to determine the FTF model parameters instead of relying on experiments. Following this approach, it is shown how to obtain the flame response for a whole range of frequencies with a minimum set of simulations of an unforced flame in a thermo-acoustically stable state. As a complement, an increase in the model fidelity is demonstrated by addressing a reduced set of acoustically forced simulations in addition to the stable steady case. This would constitute a considerable improvement for the FTF determination over classical methods such as using nu-

merous forced LES, or even more advanced techniques relying on system identification [31] which are limited to vanishingly small perturbations.

In the following, a description of the model for the FTF of a swirled V-shaped flame is first presented in Section 2, the role of each parameter being discussed. The lean premixed swirled flame configuration is then presented in Section 3. LES predictions are validated against experimental data for cold and reactive conditions in Section 4, followed by a first estimation of the FTF. It is shown that qualitative agreement for the FTF gain and phase is obtained when extracting parameters from an unforced flame simulation. Finally, in Section 5, flame dynamics as obtained in acoustically forced LES are validated against experimental results and more accurate evaluation methods for model parameters estimations are proposed. Model and experimental flame responses are finally compared, demonstrating the ability of the methodology to predict the FTF gain and phase with a good accuracy.

2. Flame transfer function modeling and theory

Many analytical expressions for the FTF based on a linearization of the G-equation have been derived since the pioneering work from Fleifil et al. [32] for the frequency response of a conical laminar premixed axisymmetric flame stabilized on a tube rim which is submitted to harmonic flow-rate modulations. Assuming that the flame is a thin interface separating fresh and burnt gases and moving at the laminar flame speed s_f in the direction normal to its surface, what is generally described by a G-equation, Fleifil et al. [32] were able to derive an analytical expression for an elongated conical flame primarily depending on a flame Strouhal number. The vast majority of analytical FTF models in the literature was then also derived from an analysis involving a perturbed G equation whether it be in a general laboratory frame or in a frame linked to the mean flame front position for conical or V-shaped flames. In the following, focus is made on V-shaped flames like the one described in Fig. 1. Local flame wrinkling is assumed to occur around this mean position which does not change when acoustic forcing is applied, which translates for a premixed flame to only considering linear acoustics [33].

For the model derivation, although alternatives exist [34], we make use here of the convective model for laminar V-shaped flames introduced by Schuller et al. in [30] and where a convective velocity perturbation propagates in the vertical direction in the laboratory reference frame. That is:

$$v' = v_1 \exp\left(i \frac{\omega}{\bar{v}} y - i \omega t\right) = v_1 \exp(iky - i \omega t) \quad (2)$$

where $k = \omega/\bar{v}$ is a convective wavenumber built from the average axial flow speed \bar{v} and the angular frequency ω . Parameters a and b in Fig. 1 correspond to the flame anchoring point and the radial flame extension respectively. The analysis is restricted to swirled flames anchored on a narrow stabilizing rod, so that $a \ll b$. Integrating the unsteady flame displacement over the flame front and considering that the unsteady heat release rate is directly proportional to the unsteady flame surface variation, Schuller et al. [30] obtain the analytical FTF reproduced below for convenience:

$$\mathcal{F}_v = \frac{2}{\omega_*^2} \frac{1}{1 - \cos^2 \alpha} \left[e^{i\omega_*} - 1 - \frac{e^{i\omega_* \cos^2 \alpha} - 1}{\cos^2 \alpha} \right] + \frac{2i}{\omega_*} \frac{1}{1 - \cos^2 \alpha} \left[e^{i\omega_* \cos^2 \alpha} - e^{i\omega_*} \right] \quad (3)$$

where $\omega_* = (\omega R_f)/(s_f \cos \alpha) = (\omega L_f^2)/(\bar{v} H_f) = (\omega L_f)/(\bar{v} \cos \alpha)$ is a non-dimensional reduced frequency related to the flame Strouhal number of Fleifil et al. [32] and $\alpha = \sin^{-1}(s_f/\bar{v}) = \cos^{-1} H_f/L_f$ is a flame aspect ratio parameter or simply the flame angle with respect to the main flow direction, related to the laminar flame

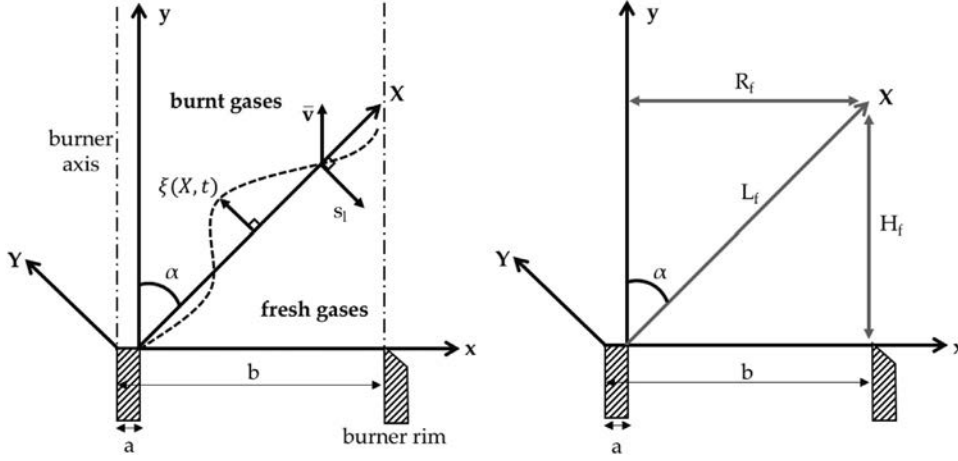


Fig. 1. Schematic of the studied V-shaped flame configuration. Reference frame axes are noted x and y while a second frame directly linked to the steady flame has axes X and Y . The steady flame is aligned on the X axis. It is anchored on a rod at position a and extends to a radial abscissa $x = b$ which may not be a wall. Definitions of the flame length L_f , flame height H_f and flame radius R_f are provided on the right (adapted from [30]).

speed s_l . The ratio ω^*/ω represents the convection time from the anchoring point to the extremity of the flame sheet at the mean flow velocity. This first expression solely depends on mean flow and geometrical quantities, which is not surprising in the context of laminar flames it was originally developed for, but raises questions for turbulent flames where dynamics are likely to be of crucial importance. As pointed out by Preetham et al. in [35], a limitation of this model stems from the fact that the convective velocity in Eq. (2) assumes that perturbations travel at the mean flow velocity \bar{v} . In reality these perturbations (that we will assimilate to vortical perturbations to simplify the analysis) travel in the outer shear layer in the case of a V-shaped flame at a velocity U_{c-v} that may be lower than \bar{v} [36] but cannot exceed it. Introducing the true to mean velocity ratio K , one therefore necessarily has $K = \frac{\bar{v}}{U_{c-v}} \geq 1$. Eq. (2) can accordingly be modified by adding the correction factor K to the wavenumber, which yields the following expression for the FTF:

$$\mathcal{F}_v = \frac{2}{\omega_*^2} \frac{1}{1 - K \cos^2 \alpha} \left[e^{i\omega_*} - 1 - \frac{e^{i\omega_* K \cos^2 \alpha} - 1}{K \cos^2 \alpha} \right] + \frac{2i}{\omega_*} \frac{1}{1 - K \cos^2 \alpha} \left[e^{i\omega_* K \cos^2 \alpha} - e^{i\omega_*} \right] \quad (4)$$

A potential drawback for the model as is, especially for wide flame angles, is that it may result in large gain values for high frequencies which are not observed in experiments for this type of flames [37]. Indeed Schuller et al. [38] show by use of PIV measurements in the fresh gases that the velocity perturbation amplitude decreases with the axial distance, with a frequency dependent decay rate. The authors also pointed out that this feature is needed to retrieve the FTF obtained experimentally when using a model derived from a G-equation. Further studies focusing on the fresh reactants side [39] found velocity perturbations to have an exponential decay rate which increases with frequency. By construction, the FTF model \mathcal{F}_v only considers one-dimensional propagation without any decay, which may be true in the injection system but may not hold as the perturbation goes through the larger combustion chamber enclosure. To take this feature into account, the spatial component \hat{v} of the convective velocity $v' = \hat{v}e^{-i\omega t}$ in Eq. (2) can again be modified following the formulation proposed in [40]:

$$\begin{aligned} \hat{v} &= v_1 \exp\left(i \frac{K\omega}{\bar{v}} y\right) \exp\left(-\beta \frac{K\omega}{\bar{v}} y\right) \\ &= v_1 \exp\left(i \frac{K(1+i\beta)\omega}{\bar{v}} y\right) \end{aligned} \quad (5)$$

which effectively comes down to introducing a new complex velocity correction factor $K' = K(1 + i\beta)$ instead of a real-valued quantity. In this case, the corresponding decay rate, $-\beta K\omega/\bar{v}$, increases with frequency which complies with experimental findings. This means that Eq. (4) retains the same form, and in the latter, the parameter K is always assumed to be complex for conciseness purposes.

To this point, \mathcal{F}_v holds for a laminar V-shaped flame without any consideration regarding swirl or any azimuthal velocity component. Analytical expressions for swirling flames are much more scarce than for standard laminar flames. The model presented here is a slightly modified version of the expression introduced by Palies et al. [28] for swirling V-shaped flames. It has already been applied with some success in [41] to gain insight on the dynamics of stratified swirling flames. Palies et al. [28] show that the swirling flame FTF can be written as:

$$\mathcal{F}_s = \mathcal{F}_v \left[1 - \frac{\hat{s}_t/\bar{s}_t}{\hat{v}/\bar{v}} \right] \quad (6)$$

where \mathcal{F}_v is the laminar V-shaped flame FTF that was previously detailed and s_t is the turbulent flame speed. According to Palies et al. [28], turbulent velocity fluctuations are assumed to be linked to the normalized velocity fluctuations in a linear fashion using two real valued model parameters χ and ζ so that:

$$\frac{\hat{s}_t}{s_t} = \chi \frac{\hat{u}_\theta}{\bar{u}_\theta} + \zeta \frac{\hat{v}}{\bar{v}}, \quad (7)$$

The axial \hat{v} and azimuthal \hat{u}_θ velocity disturbances are then assumed to be related by:

$$\frac{\hat{u}_\theta}{\bar{u}_\theta} = \frac{\hat{v}}{\bar{v}} e^{i\phi_{\hat{u}_\theta-\hat{v}}} \quad (8)$$

This means that the normalized velocity fluctuations are essentially the same but with a phase shift $\phi_{\hat{u}_\theta-\hat{v}}$ between the axial and the azimuthal components. Reintroducing Eqs. (7) and (8) in Eq. (6) then yields the FTF for a swirling V-shaped flame :

$$\mathcal{F}_s = \mathcal{F}_v \left[1 - \left(\zeta + \chi e^{i\phi_{\hat{u}_\theta-\hat{v}}} \right) \right] \quad (9)$$

which depends on six parameters : ω_* , α , K , χ , ζ and $\phi_{\hat{u}_\theta-\hat{v}}$. In the original work of Palies et al. [28], no additional constraint is present. One can however point out that according to theory, the FTF gain at zero frequency should always be unity [42]. Setting $\phi_{\hat{u}_\theta-\hat{v}} = \omega\tau$ where τ is a characteristic time delay between axial acoustic and azimuthal convective velocity perturbations, imposes

$\chi = -\zeta$. The other solution $\chi = 2 - \zeta$ is discarded as it yields non physical results. This simplistic assumption does however not hold when confronted to the experimental findings from [28]. Introducing a more general framework by setting $\phi_{\hat{u}_\theta - \hat{v}} = \omega\tau + \phi_0$ and enforcing the low frequency limit gain yields:

$$|1 - \zeta + \chi e^{i\phi_0}| = 1 \quad (10)$$

where $|\cdot|$ stands for the modulus of a complex number. It results a second order equation relating χ and ζ :

$$\zeta^2 + 2\zeta(\chi \cos \phi_0 - 1) + \chi^2 - 2\chi \cos \phi_0 = 0 \quad (11)$$

Assuming χ and ϕ_0 to be known, solutions of this equation are:

$$\zeta_1 = 1 - \chi \cos \phi_0 + \sqrt{1 - \chi^2 \sin^2 \phi_0} \quad (12)$$

$$\zeta_2 = 1 - \chi \cos \phi_0 - \sqrt{1 - \chi^2 \sin^2 \phi_0} \quad (13)$$

Assuming $|\chi| \leq 1$, ζ_1 and ζ_2 take real values. Without any data to compare the model results, and depending on parameter values, it is difficult to choose between one root or another. Experiments for V-shaped flames FTF have shown that such flames exhibit an increase in gain in the low frequency limit [37]. Starting from Eq. (9) and inserting Eq. (12) or (13), one can show after some calculus that to first order, the low frequency derivative for the FTF gain reads:

$$\lim_{\omega \rightarrow 0} \frac{\partial |\mathcal{F}_s|}{\partial \omega} = \tau \sin \phi_0 \left[\chi^2 \cos \phi_0 \pm \chi \sqrt{1 - \chi^2 \sin^2 \phi_0} \right] \quad (14)$$

Therefore, the value ensuring a positive derivative of the FTF gain in the low frequency limit is chosen depending on values for χ , τ and ϕ_0 . Eq. (9) along with Eq. (12) or (13) constitute the parametrization of a V-shaped premixed swirling flame transfer function that will be referred to as the SFTF model throughout the rest of the article. This model relies on a set of six independent parameters, three of which describe the premixed flame response (ω_* , α , and K) while the three remaining ones account for the effect of the swirling motion (χ , τ and ϕ_0). While the current model is limited to premixed V-shaped flames, it could handle various flow injection conditions and fuels through parameters ω_* and α while various swirler designs would affect parameters τ , ϕ_0 and χ . Note that an overview of the role of each parameter is available in supplemental material A in the form of a sensitivity analysis. From this study, it is concluded that every investigated parameter should be evaluated with caution, and emphasizes both the need for an accurate description of flame dynamics as well as for a precise evaluation of intermediate quantities needed to evaluate model parameters. This evaluation process should ideally be robust enough to cover a large spectrum of configurations.

3. Test configuration and modeling

To proceed with the SFTF model validation, LES of a generic configuration are performed. In this matter, a laboratory scale premixed swirl stabilized burner is chosen as it features a turbulent swirling flow and an easy to model geometry. The numerical setup is conceived to be robust enough to allow focus on the evaluation of quantities of interest with reduced relative uncertainties. Details regarding the experimental rig and the numerical modeling strategy are presented in the following section.

3.1. Experimental setup

The experimental configuration used for analysis and model development is a variation of the NoiseDyn burner already studied in [43–46]. The rig is composed of an injection system, a swirler unit

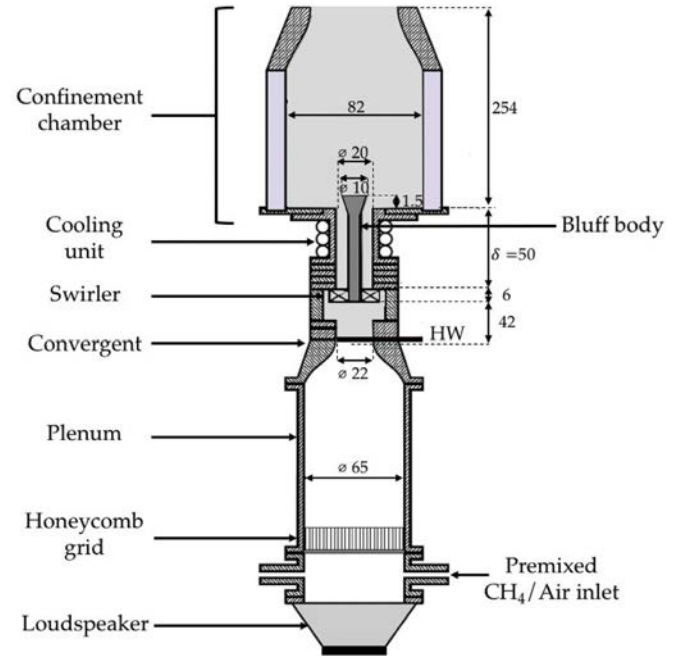


Fig. 2. Sketch of the NoiseDyn swirl combustor, with dimensions in mm. Only the shaded domain is resolved in the LES, starting 6 mm under the hot wire position (HW). δ is the distance between the combustion chamber backplane and the top of the swirler channels exit.

and a combustion chamber ending with a short exhaust tube as presented in Fig. 2. A premixed methane/air mixture of equivalence ratio $\phi = 0.82$ is injected through the bottom of the device and passes through a honeycomb layer to break large turbulent eddies, the system being operated at $P_0 = 1$ atm and with a fresh gases temperature $T_0 = 293$ K. The resulting laminar flow enters a 65 mm wide plenum and a convergent of diameter $D_{in} = 22$ mm, producing a top-hat velocity profile with bulk velocity $U_b = 5.44$ m/s at the hot wire position identified as HW in Fig. 2. The flow then goes into a radial swirler using six cylindrical channels of diameter $d_{sw} = 6$ mm forming a 33° angle with respect to the radial direction, before leaving through a central 20 mm wide injection tube. The injection also includes a central metallic rod of diameter $d = 6$ mm topped by a 10 mm high truncated cone ending with a circular section of diameter $D_c = 10$ mm to help stabilizing the flame. Note that the cone is protruding 1.5 mm inside the combustion chamber and the chamber back-plane to swirler back-plane distance is $L_{bc} = 56$ mm. The combustion chamber itself is 150 mm long, is equipped with four quartz windows and has a square cross-section of $L_{ch} = 82$ mm width. In the absence of acoustic forcing, the flame is anchored few millimeters above the cone and has a V shape.

This academic configuration is not as complex as injectors used in real engines, yet it includes their most prominent features with a turbulent swirling flow and confined flame operated at lean premixed conditions. It allows for an easier interpretation of LES results than in real scale burners. A wide selection of diagnostics has been employed by Gatti et al. [47,48], including velocity measurements with a hot wire, pressure measurements using microphones, LDV and PIV of the flow at the injection exit and in the flame residence area. FDF data is available for forcing amplitudes ranging from 10 to 70% RMS of the bulk velocity at the hot wire location. In the following, only the unforced data and the one at a forcing amplitude $v'_{RMS} = 30\%$ is considered.

Table 1

List of meshes created during the adaptation process and their characteristic dimension h in the swirler, injector and flame regions.

Mesh id.	h_{swirler} (mm)	h_{injector} (mm)	h_{flame} (mm)	number of tetrahedra
M1	0.306	0.379	0.515	15 526 871
M2	0.253	0.327	0.515	16 234 106
M3	0.251	0.290	0.476	19 110 948
M4	0.158	0.197	0.260	55 766 260

3.2. Numerical modeling

LES of the configuration described in the previous subsection are performed using the AVBP solver developed by CERFACS, which solves the three-dimensional filtered compressible multi-species Navier–Stokes equations on unstructured grids. The TTGC centered spatial scheme [49] is used, featuring a third order accuracy in both space and time. The computational domain covers a region starting after the plenum contraction all the way to the exit of the exhaust tube to reduce the total cost of the simulation. Since the flame response to acoustics is to be studied, characteristic boundary conditions [50] are used for both inlet and outlet, ensuring a proper treatment of waves. All other boundary conditions are set to adiabatic no slip walls for the cold flow simulations, while for hot conditions, chamber walls as well as the conical part of the stabilizing rod are specified as heat losing walls. To do so, experimental temperature measurements outside of the quartz panels are used as a reference along with adequate thermal resistances, allowing wall temperatures in the LES to adapt to the chamber temperature field. The conical bluff-body is assumed to have a constant temperature of 293 K at its base inside the injection unit and the fin theory is used to derive a space dependent analytical expression for the thermal resistance. Since few experimental data is available for the combustion chamber back plane temperatures, a hyperbolic tangent profile varying between 300 K in the central watercooled region to 700 K near the chamber walls is prescribed. Finally, the SIGMA subgrid scale model is used [51] while flame/turbulence interaction is handled using the Dynamically Thickened Flame model (DTFLES [52]) in conjunction with a two-step BFER chemistry [53] validated for atmospheric conditions.

For meshing, the mesh adaptation strategy proposed by Daviller et al. [54] is employed, resulting in three meshes M1, M2, M3 presented in Table 1, where h is the characteristic cell size in a particular mesh area.

To proceed, a baseline full tetrahedra unstructured mesh, M1, was first created, with refined regions around the swirler, the injection system and the area where the flame is supposed to stabilize. The normalized time averaged viscous dissipation defined by:

$$\overline{\Phi} = (\mu + \mu_t) \left(\frac{\partial u_i}{\partial x_j} + \frac{\partial u_j}{\partial x_i} \right)^2 \quad (15)$$

where μ and μ_t are the laminar and turbulent dynamic viscosities respectively was then extracted from the associated LES predictions and used as a metric for the automatic mesh refinement process. It results a new mesh, M2, from which the process is iterated once again to yield mesh M3. This method allows not only to adapt the mesh near walls to reach acceptable values of normalized wall distances y^+ , but also improves pressure loss predictions across the swirler, which is of particular importance for the determination of the phase between acoustic and vortical perturbations, $\phi_{\hat{u}_\theta - \hat{p}}$. As a result, a 2% error on the swirler pressure loss with M3 is obtained if compared to experiments (see Table 2).

In terms of mesh adaptation, Table 1, one can observe that the transition from M1 to M2 reduced the characteristic length scale

Table 2

Mean pressure loss obtained with meshes M1, M2, M3 and in experiments. For numerical simulations, the mean pressure loss is calculated as the difference between the inlet and outlet surface averaged pressures.

Case	$\Delta P_{\text{swirler}}$ (Pa)	difference with Exp. (%)
M1	465	39
M2	364	9
M3	341	2
Exp.	335	NA

within the swirler, while the transition from M2 to M3 mainly impacted the injector and flame regions. To further validate M3, a fourth mesh M4 was also created to assess mesh invariance in reactive simulations. For that purpose, mesh characteristic length scales in the swirler, injector and flame regions have been divided by two compared to M1, yielding lower characteristic length scales in these regions (see Table 1) but also comparable local refinement compared to M3. As a result and despite an increase in the computing power needed to achieve the same physical time, only minor differences were observed between M3 and M4. The reader is referred to supplemental material B for further details. As a consequence and unless told so, all results presented in the following are obtained from simulations based on mesh M3.

4. FTF assessment from stationary flame data

4.1. Numerical setup validation against experimental data

In the following, LES results based on mesh M3 are first compared to experimental data in non reacting conditions to assess the reliability of the numerical setup prior to any combustion simulation. As already shown in the last section, pressure losses across the swirler are in very good agreement with experiments. LDV measurements available from experiments over a line located 3 mm above the chamber backplane are used to gauge the numerical prediction. It is worth noting that measurements were obtained without the enclosing chamber walls, while simulations are always fully enclosed. For comparison, LES data is averaged over 137 ms, i.e. approximately 8.6 inlet to injector backplane flow through times. Data are furthermore averaged in the azimuthal direction since the injector diameter to chamber width ratio is low, resulting in a quasi axisymmetric flow. Results presented in Fig. 3 show a very good agreement with experimental data for all mean velocity components. A slight overestimation of the axial velocity peaks is present, as well as minor discrepancies when $x/R > 1$ for radial and azimuthal velocities, $R=10$ mm being the injector outer radius. RMS velocity components, Fig. 3(d)–(f) are also in good agreement in the central region where the first series of peak is captured by LES. Again, discrepancies are visible in the outer shear layer ($x/R > 1$) where only the RMS of axial velocity is observed to properly match the experiment. The estimated swirl number from LDV measurements is 0.8 while the LES yields $S = 0.73$. All these minor differences can be attributed to the unconfined experimental measurements versus confined simulations. Another possible explanation lies in the fact that LDV measurements are known to introduce a small bias for turbulent flows [55], and the discrepancies observed here are localized in the turbulent region that is the outer shear layer. Further validation is available in supplemental material C. Overall, LES captures the investigated configuration swirling flow features with satisfactory agreement, allowing to proceed to the reacting conditions with confidence.

In its steady state reacting regime, LES as well as experimental observations indicate that the flame has a classical V shape and is stabilized few millimeters above the central bluff

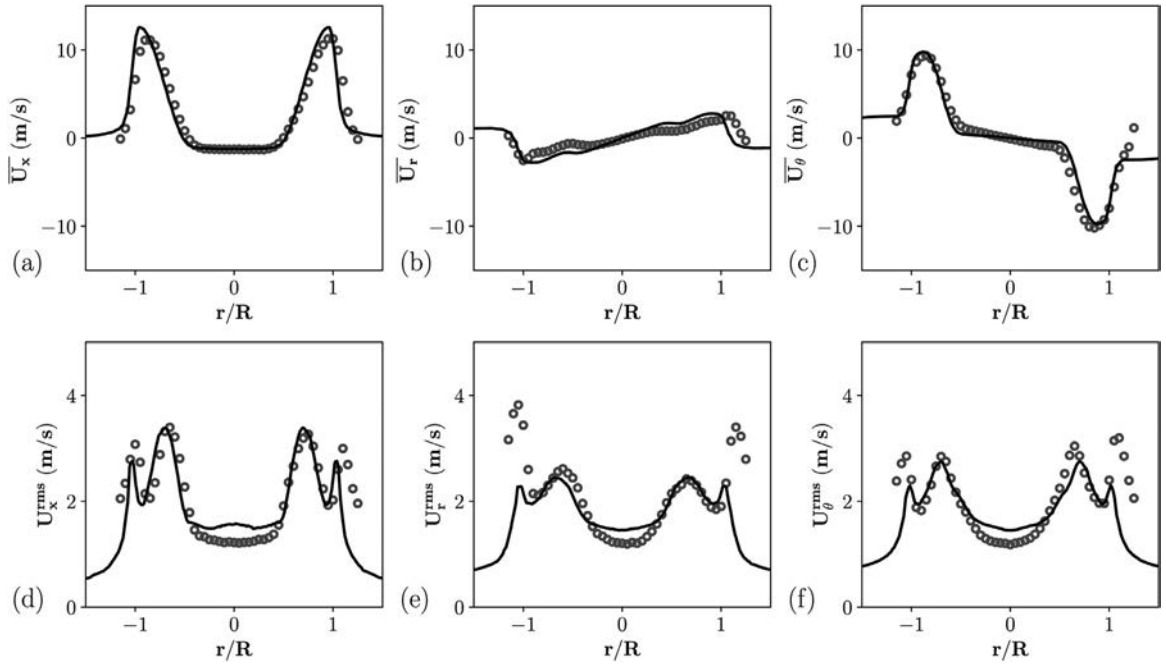


Fig. 3. Comparison of velocity fields under cold flow conditions measured with LDV (\circ) and obtained in LES (—), 3 mm above the chamber back plane. (a), (b) and (c) : mean values, (d), (e) and (f) : RMS values of axial (left), radial (middle), and azimuthal (right) velocity components. Axial distance is normalized by the injector radius $R = 10$ mm.

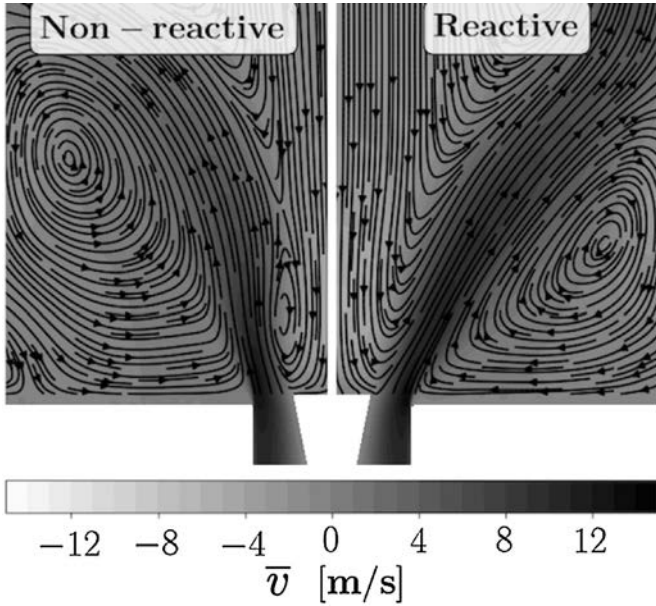


Fig. 4. Non-reactive (left) and reactive (rights) axial velocity fields and velocity streamlines. Combustion strongly affects the flow and widens the inner recirculation zone.

body. The flow structure downstream the injector is of course drastically modified by the presence of the flame in comparison to cold flow conditions. The expansion of the burnt gases increases the flow velocity near the flame, pushing the flow outer recirculation zones downwards while the inner recirculation zone becomes bigger than in the non-reacting case. As a result, Fig. 4 shows that the flow angle at the injector exit slightly increases. Figure 5 presents the heat release rate distribution on a vertical plane in the middle of the chamber, obtained from LES fields averaged over time (80 ms) and in the azimuthal direction, complemented by an Abel transform of OH^* signals from the experiment.

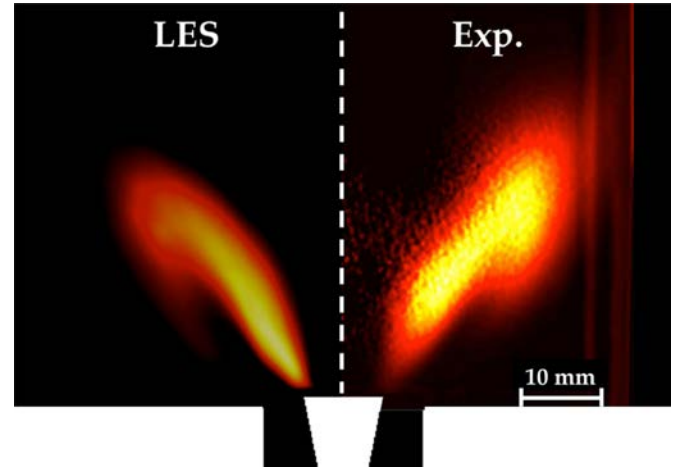


Fig. 5. Comparison of steady state flame shapes. On the left, LES heat release rate field averaged over 80 ms. On the right Abel transform of OH^* signal recorded by a CCD camera with a narrowband filter centered around 310 nm, averaged over 100 samples.

For the numerical simulation, the normalized heat release rate averaged in the azimuthal direction and over 80 ms is used, the normalization value being the maximum value found in the simulation. Clearly, numerical and experimental flame shapes are in good agreement, though a minor difference in flame height can be observed and may possibly be explained by the limited thermal data available for the LES to match the experiment. Indeed, in experiments the flame exhibits a larger lift-off distance than in LES, which may imply that the bluff-body tip temperature is lower than the value estimated from simulations. The mean flame angle is also well reproduced by the simulation. Secondary branches on the upper part of the flame found in the experiment are reproduced numerically, showing that thermal conditions necessary to the flame stabilization are correctly reproduced by the LES [56,57]. Further comparisons using PIV data on a vertical plane 3.5 mm above the

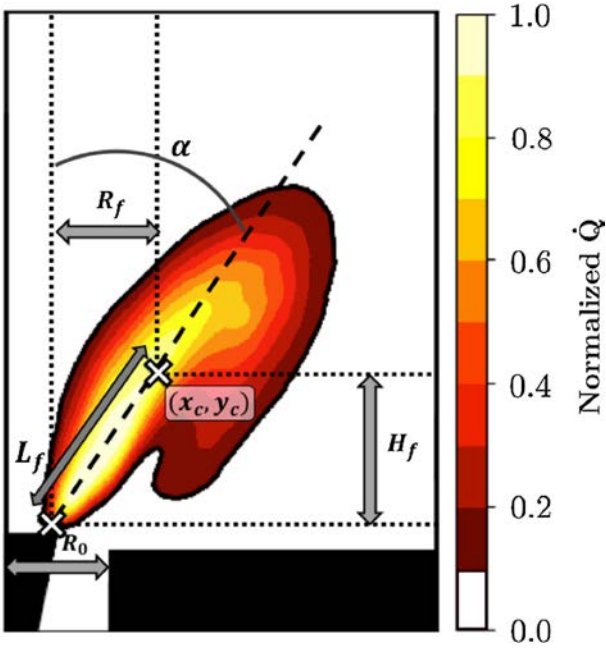


Fig. 6. Schematic of the flame and associated quantities of interest : α , L_f , H_f , R_f , R_0 . The position of the \dot{Q} center of mass (x_c, y_c) is shown.

chamber back plane are provided as supplemental material in annex D. They show a very good agreement at several locations for both mean axial and azimuthal velocities, indicating that the flow angle is indeed well captured by the simulation.

Overall, LES is able to capture both cold and reactive flow features with good accuracy, allowing to move on with confidence on to the SFTF parameters estimation step.

4.2. SFTF model parameters estimation from stationary data

LES results are used to probe geometrical quantities of interest needed to determine the reduced frequency $\omega_* = \omega L_f^2 / (\bar{v} H_f)$ as well as the half flame angle α . A wide variety of flame dimension definitions is available in the literature, the most common ones rely on isolevels of a variable representative of the flame front (typically heat release rate or a progress variable) in the case of numerical simulations. In this paper, dimensions are defined from the location of the center of mass of the heat release rate \dot{Q} field obtained from time and azimuthally averaged solutions [58]. Given N , the number of nodes in the solution, the centroid coordinates (x_c, y_c) of the heat release rate distribution in a vertical plane are given by:

$$x_c = \frac{\sum_{k=1}^N \dot{Q}_k x_k y_k}{\sum_{k=1}^N y_k \dot{Q}_k} \quad \text{and} \quad y_c = \frac{\sum_{k=1}^N \dot{Q}_k y_k y_k}{\sum_{k=1}^N y_k \dot{Q}_k} \quad (16)$$

Coordinates for the flame anchoring point are much less sensitive to its definition. It is here defined as the lowest point in the axial direction where \dot{Q} is at least superior to 1% of its maximum value. Figure 6 shows the position of the retrieved centroid of heat release rate distribution and the associated flame dimensions. For the specific configuration of this work, one gets : $R_f/R_0 = 1.0$, $L_f/R_0 = 1.75$, $H_f/R_0 = 1.44$ and $\alpha = 34.8^\circ$. The mean axial velocity at the injector exit plane $\bar{v} = 8.78$ m/s is measured from the stationary unperturbed LES to complete the analysis, yielding $\omega_*/\omega = 2.43$ ms.

The next critical step in the SFTF construction is to determine the axial convection velocity U_{c-v} of vortical structures along the outer shear layer of the swirling jet exhausting the injector. For V-

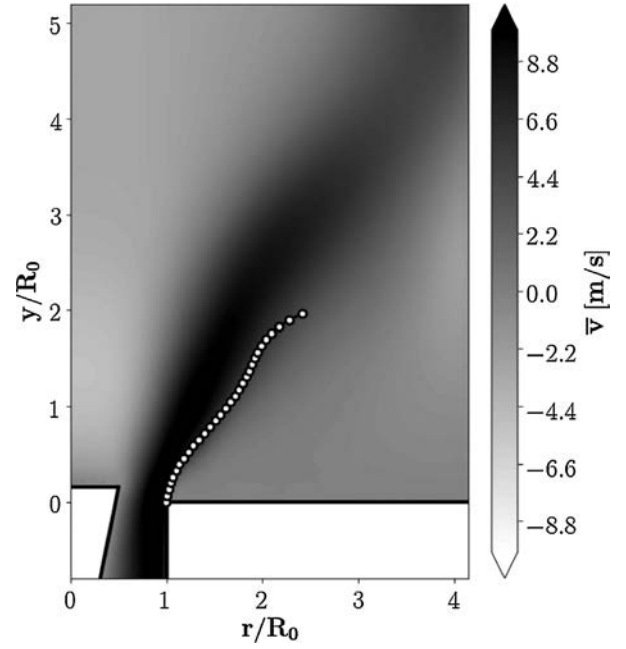


Fig. 7. Identification of the outer shear layer using the I_2 criterion for the reactive case. Each white dot represent the local maximum at a given height y/R_0 .

shaped flames like the present one, these structures are responsible for large surface area perturbations and thus, in the case of a premixed flame, for the major part of the unsteady heat release [33,36]. One possibility to assess the real speed of these disturbances is to use a tracking algorithm [59]. While theoretically appealing, this method has some limitations in a turbulent LES framework and requires acoustically pulsed simulations. Another possibility arising for highly swirling flows is to use properties coming from solid mechanics theory. For solid bodies, the norm of the second principal invariant of the deviatoric stress tensor is used as a measure of shear. In the present case, swirl is strong enough (and possibly the injection tube narrow enough) so that the angular momentum flux prevails, resulting in a fully developed turbulent pipe flow in solid body rotation. A similar criterion [60] resembling the classical λ_2 criterion for vortex identification is therefore used, that is the second invariant I_2 of the strain rate tensor S , which is in practice computed as:

$$I_2 = \frac{1}{2} S_{ii} S_{jj} - S_{ij} S_{ji} \quad (17)$$

Negative values of I_2 indicate high shear regions. Applied to the mean steady reacting field issued by LES, maximum negative values of I_2 identify a collection of abscissa starting from the injector exit up to the distance H_f associated to the height of the centroid of heat release rate distribution. This yields a curve assigned as the outer shear layer trajectory shown in Fig. 7. Note that other criteria could be used to identify the shear layer, such as the norm of the strain rate tensor, removing the possible high swirl limitation of the method. The I_2 criterion was however shown to be particularly robust for high swirling flows. Along this path, the local axial velocity at a given y abscissa is retrieved and thereafter noted $v_l(y)$. The axial velocity component of vortical structures U_{c-v} is then evaluated by averaging the axial velocity along the shear layer path over the distance H_f , that is:

$$U_{c-v} = \frac{1}{H_f} \int_0^{H_f} v_l(y) dy \quad (18)$$

where H_f is the flame height (Fig. 6). Using the available average LES fields yields $U_{c-v} = 6.46$ m/s. The real part of the correction

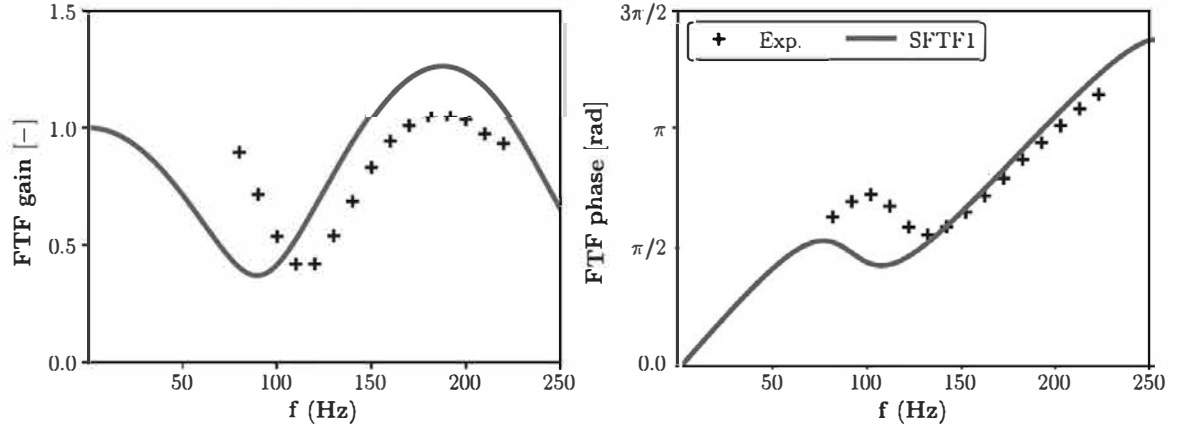


Fig. 8. SFTF1 model results with parameters estimated from a single stationary unperturbed LES : $\omega_s/\omega = 2.43$ ms, $\alpha = 34.8^\circ$, $K = 1.36$, $\chi = -0.33$, $\tau = 5.55$ ms, $\phi_0 = 0$ rad.

factor K for the FTF model therefore equals $K = \bar{v}/U_{c-v} = 1.36$. In the absence of pulsed LES data, one can estimate the time delay τ by assuming that acoustic perturbations travel at the sound speed c while azimuthal perturbations are convected at the local flow speed u_c over a distance $\delta = 50$ mm between the swirler vanes exit where acoustic/vorticity conversion occurs [29] and the injector exit plane (see Fig. 2):

$$\tau = \delta \left(\frac{1}{u_c} - \frac{1}{c} \right) \quad (19)$$

As a first approximation, the phase ϕ_0 is simply nullified. By doing so, the low frequency gain limit condition from Eq. (10) reduces to $\chi = -\zeta$ and the FTF phase is evidently forced to a null value in the zero frequency limit. Finally, choosing $u_c = \bar{v}$ as a first approximation yields $\tau = 5.55$ ms. The choice of the convective velocity u_c is still subject to discussions in the community. It has been observed experimentally [61] and while trying to reproduce FTF from models [26] that the actual value may be 40–50% larger than the bulk velocity in the injection device. Recently, Albayrak et al. [62] have proposed an analytical expression for this quantity in the low axial wavenumber limit based on a modal decomposition of the linearized Euler equations which resumes to:

$$u_c = \bar{v}(1 + 2\kappa/\lambda_0) \quad (20)$$

where κ is the circulation strength of the swirling flow and λ_0 is the first eigenvalue of a characteristic Sturm-Liouville equation. Applied to the current configuration, the above expression yields $u_c = 1.55\bar{v}$ with $\kappa = 1145 \text{ s}^{-1}$ and $\lambda_0 = 470$, resulting in $\tau = 3.51$ ms which does not comply with the time delay found in the LES as will be presented in Section 5. For this reason, it was chosen to use $u_c = \bar{v}$. No information is available for the determination of the swirl fluctuation intensity parameter χ . In the present paper and as a first step, a value comparable to those found in [28,41] is used : $\chi = -0.33$.

From the parameters estimated previously, one can obtain a first estimation of the flame acoustic response, that is denoted as SFTF1 and is shown in Fig. 8. With only a single stationary flame simulation, the model is able to depict the FTF gain and phase tendencies over the frequency range of interest. In particular, correct phase tendencies are already retrieved without the introduction of unsteady perturbations, and values match the experiment for $f \geq 150$ Hz. The frequency of the first local FTF gain minimum is however not retrieved using SFTF1, which also shows in the phase curve where the phase shift region is not well predicted. This point is further detailed in the next section.

5. Forced simulations for more accurate SFTF predictions

5.1. Acoustically pulsed LES results

In this section, focus is made on obtaining the parameters ϕ_0 , χ and β which require at least one acoustically pulsed simulation since they are related to dynamic features: the phase lag between acoustic and convective perturbations, swirl fluctuations intensity, velocity disturbances decay. Building upon previous simulations, and for verification purposes, pulsed LES have been performed to assess the CFD capability to successfully capture the flame response to flow perturbations. For these cases, the inlet boundary condition is changed to impose a uniform velocity pulsation with a 30% RMS amplitude, corresponding to 2.3 m/s variations, with a unique frequency in the range 80–200 Hz. NSCBC relaxation coefficients are set to low values to avoid any unwanted acoustic reflection [63]. Flame dynamics during a forcing cycle is well retrieved as indicated for $f = 180$ Hz in Fig. 9, by comparing azimuthally and phase averaged heat release rate fields with OH* chemiluminescence data at various instants in the forcing cycle. In particular, the flame angle and dimensions as well as the roll-up motion at the flame tip are well reproduced.

The FTF as obtained from single frequency LES forcing is presented in Fig. 10 and shows excellent agreement with reference data from the experiments. The characteristic low and high FTF gain regions of a swirled V-shaped flame anchored on a bluff-body are well retrieved. It is therefore concluded that LES is able to capture pulsed reactive flow features with good accuracy.

5.2. SFTF model parameters estimation from pulsed LES

To the exception of χ , all SFTF parameters can be roughly estimated from a stationary reactive simulation without acoustically forcing the flow, giving a first estimation of the flame acoustic response. It is shown in this section that performing a few or even only one additional pulsed simulation to obtain further information can improve the model accuracy. This method avoids numerous single frequency forced simulations [20,21] or the need for other identification techniques [18,64]. In addition, since quantities of interest only concern the injection system at the exit plane, which may only be marginally affected by burnt gases expansion, a single non reactive forced simulation may be sufficient for some of these parameters.

As an alternative minimizing the number of assumptions (Eq. (19)), the phase ϕ_{a-p} between acoustic and convective perturbations can also be determined from a set of pulsed flow simulations. Such a study would of course defeat the purpose of

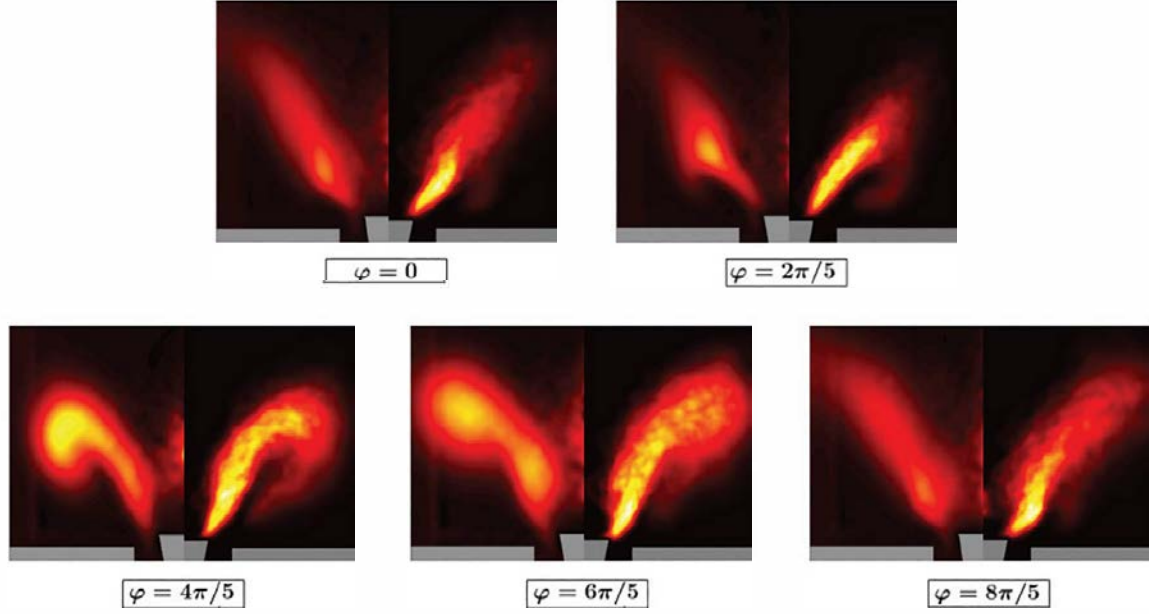


Fig. 9. Abel transform of phase averaged OH^* chemiluminescence pictures from experiments (left parts) and phase averaged field of normalized heat release rate from LES (right parts) for a forcing frequency $f = 180$ Hz. Here the experimental results were obtained with a cone protruding 1 mm higher in the chamber, but should however still be comparable. The phase φ is defined from the velocity signal at the hot wire position : $\varphi = 0$ corresponds to null acoustic velocity while $\varphi = \pi/2$ corresponds to a maximum.

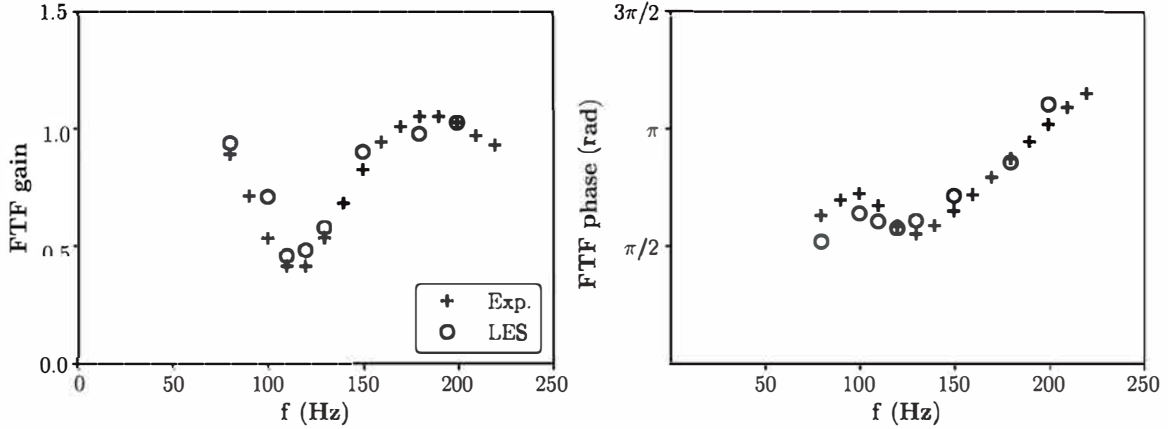


Fig. 10. Flame transfer function of the NoiseDyn burner : gain (left) and phase (right). Single frequency pulsed LES data (grey circles) is compared to experimental measurements (black crosses). Bulk velocity $\bar{v} = 5.44$ m/s, $(\bar{v}/\bar{v})_{\text{RMS}} = 30\%$.

using an analytical model which should avoid running several costly simulations, but the study is performed as another validation test here. The phase between Fourier coefficients of axial and azimuthal unsteady velocity signals integrated on the injector exit plane is used for a set of eight forcing frequencies, giving the linear regression presented in Fig. 11. The time delay $\tau = 5.54$ ms and phase at the low frequency limit $\phi_0 = 0.03$ are found to be very close to those obtained using the simple one-dimensional propagation model from Eq. (19) leading to $\tau = 5.55$ ms [29]. This result may however not be satisfactory since the first local gain minimum lies around $f = 120$ Hz and the maximum gain deviation is attained when swirl fluctuations are maximal, that is for $\phi_{\theta-\bar{v}} = \pi$ [65]. Using Eq. (19) shows that a value close to $\tau = 1/(2f) = 4.17$ ms would be expected if $\phi_0 = 0$. In [28], $\phi_{\bar{u}_{\theta}-\bar{v}}$ was evaluated experimentally at the base of the flame for different bulk velocities, reporting values of -1 and -1.5 rad for ϕ_0 with forcing frequencies going as low as 30 Hz. It is then important to notice that velocity profiles plotted in Fig. 12 are not flat at the injector outlet,

and that considering only bulk quantities may not be satisfactory. Indeed, swirl fluctuations should be considered where they preponderantly affect the flame. In the particular case of the NoiseDyn confined swirled V-flame, this region is the edge of the injector wall where large vortical structures are created and travel along the shear layer and perturb the flame surface. Accordingly, one can see ϕ_0 as a phase lag between the bulk oscillation signals and signals obtained at a particular radial location close to the wall, here chosen as a point 0.5 mm away from the injector wall on the injector exit plane, see Fig. 12. It can be evaluated as:

$$\begin{aligned} \phi_0 &= \phi_{\bar{u}_{\theta}-\bar{v}}(y_{inj}, 0.95R_0) - \frac{1}{S_e} \int_{S_e} \phi_{\bar{u}_{\theta}-\bar{v}}(y_{inj}, r) dS_e \\ &= \phi_{\bar{u}_{\theta}-\bar{v}}(y_{inj}, 0.95R_0) - \omega\tau \end{aligned} \quad (21)$$

where S_e designates the cross section area at the burner outlet y_{inj} . A maximum deviation of less than 10% in ϕ_0 is obtained when the probe position changes by 0.3 mm. Larger deviations are seen when using locations closer to the wall, depending on the local

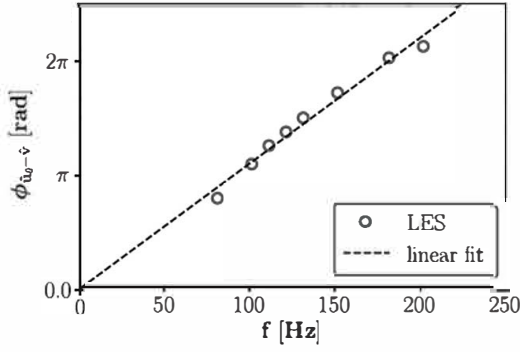


Fig. 11. Phase between axial acoustic (v') and azimuthal convective (u'_θ) velocity perturbations at the injector exit plane from surface averaged data for different pulsed LES frequencies.

Table 3
Phase ϕ_0 as obtained from LES data for different frequencies using Eq. (21).

f [Hz]	100	120	150	180
ϕ_0 [rad]	-0.832	-0.905	-0.887	-0.874

mesh size. Using data from forced LES, one gets the results of Table 3, which tend to validate the assumption that ϕ_0 is almost frequency independent in the studied pulsation range.

This means that this quantity can be obtained using only a single pulsed simulation. The signals used to obtain these values are shown in Fig. 13, with ϕ_0 computed as $\phi_0 = \phi_p - \phi_b$ using the figure notations. Inverting the equality $\phi_{a_0-\phi} = \pi$ with the newly obtained values yields an evaluation of the frequency f_1 corresponding to the FTF minimum gain:

$$f_1 = \frac{1}{2\tau} - \frac{\phi_0}{2\pi\tau} \quad (22)$$

For $f = 120$ Hz and $f = 180$ Hz respectively, Eq. (22) yields $f_1 = 115$ Hz and $f_1 = 116$ Hz, which agrees well with the frequency range $110\text{ Hz} \leq f_1 \leq 120\text{ Hz}$ obtained in the experiment, Fig. 10.

The last remaining parameter is the swirl intensity parameter χ . Although its effect on the model is quite straightforward, it is still unclear how to directly measure it using either experiments or LES. To remedy this situation, and since at least one acoustically forced reacting LES has to be performed to retrieve other model parameters dealing with the system dynamics, it is proposed to perform a pointwise optimization on both the FTF gain

and phase at a particular frequency to determine a suitable value for χ . Best agreement can only be achieved when using frequencies corresponding to local extrema of the FTF gain. Since the first local gain minimum frequency is known from the previous step, one can perform LES at this particular frequency and use it as a target. One advantage for using the lowest frequency known extremum lies in the fact that at this stage, no high frequency acoustic decay is taken into account and thus, the obtained χ value is more likely to be a good estimate. Once again, it is made use of the data of the pulsed LES at $f = 120$ Hz in conjunction with an optimization algorithm to determine the best value for the SFTF model to match the FTF gain and phase as obtained from LES at this particular frequency. The value $\chi = -0.368$ is obtained as the optimal one.

With the addition of ϕ_0 and the optimization process on χ , the SFTF model reaches a higher level of complexity, here denoted as SFTF2 and shown in Fig. 14.

5.3. SFTF model with a spatial decay for velocity disturbances

Finally, the spatial decay rate of the velocity perturbation amplitude, β , can be evaluated by means of a single pulsed cold flow simulation with the same 30% RMS amplitude as in the reactive case presented in the previous section. The FTF model derivation was done assuming a clear separation between fresh and hot gases, which is obviously not the case for a confined swirl burner where outer recirculation zones contain hot gases. For this reason cold flow simulations were preferred to determine β . In this case, two forcing frequencies are investigated: $f = 120$ Hz and $f = 180$ Hz corresponding to the identified local minimum and maximum amplitudes of the FTF gain (Fig. 10). Velocity disturbance amplitudes are probed on a vertical line at $r/R_0 = 0.75$ which corresponds to the central line between the injector outer wall radius and the conical bluff body top radius as shown in Fig. 15(a). Figure 15(b) shows that LES predicts a decrease of the amplitude as expected from experiments.

Post-processing the LES data leads to $\beta = 0.184$ for $f = 120$ Hz and 0.188 for $f = 180$ Hz. These specific values were obtained by fitting an exponential function of the form $Ae^{-\gamma y}$ so that $\beta = \gamma \frac{U_{c-v}}{\omega}$ where $U_{c-v}|_{cold} = 3.83$ m/s comes from the technique described in Section 4 for the unperturbed cold LES fields. Embedding the decay rate in the SFTF model should allow for better gain prediction at relatively high frequencies. In the following it is chosen to proceed with the value obtained for $f = 120$ Hz as this particular frequency was already studied for reacting conditions. The optimal value for χ is of course not the same with the spatial decay com-

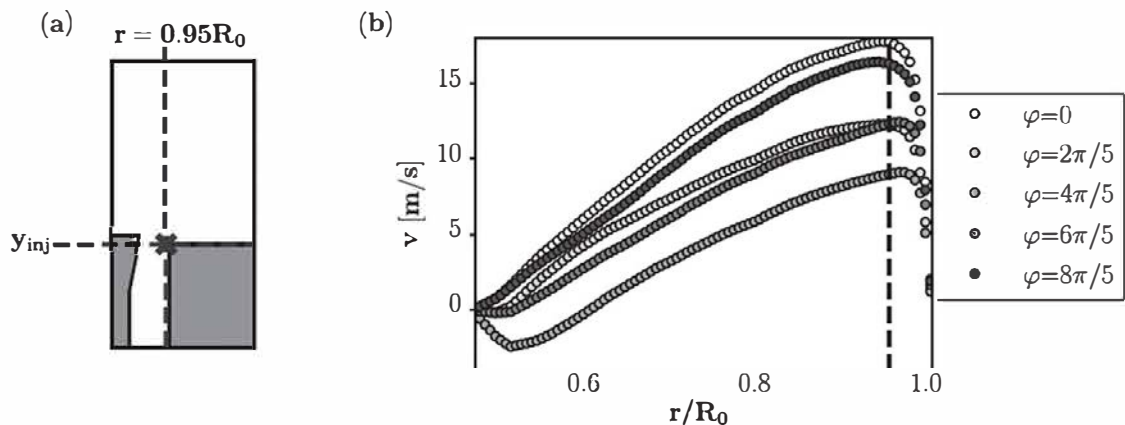


Fig. 12. (a) Sketch of the burner with the position of the integration surface height marked as y_{inj} and the probe near the outer wall represented by a black cross, located 0.5 mm away from the wall. (b) Axial velocity profile at axial position y_{inj} for different phases of the forcing cycle ($\varphi = 0$ corresponds to a maximum velocity at the hot wire position); time evolving non homogeneous profiles indicate that there may be a phase shift between the bulk signal oscillation and the oscillation at $r = 0.95R_0$.

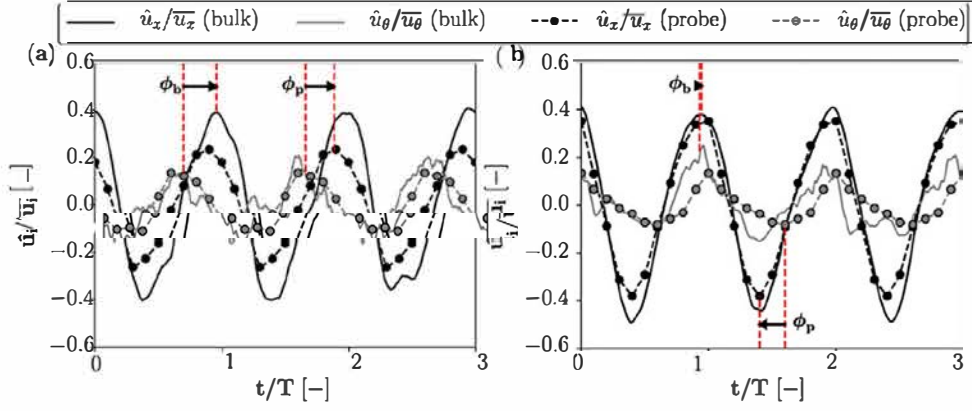


Fig. 13. Normalized axial and azimuthal velocity signals on the injector exit plane (bulk, solid line) and on a probe 0.5 mm away from the outer injector wall (dashed line with markers) for (a) $f = 120$ Hz and (b) $f = 180$ Hz. These signals correspond to $\phi_0 = -0.905$ rad and $\phi_0 = -0.875$ rad respectively, with $\phi_0 = \phi_p - \phi_b$.

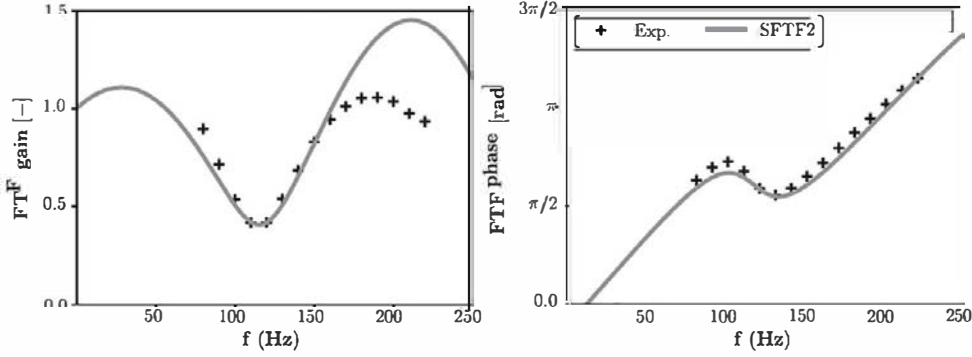


Fig. 14. SFTF2 model results with parameters estimated from a stationary LES and an additional reactive forced LES at $f = 120$ Hz : $\omega_s/\omega = 2.43$ ms, $\alpha = 34.8^\circ$, $K = 1.36$, $\chi = -0.368$, $\tau = 5.55$ ms, $\phi_0 = -0.905$ rad.

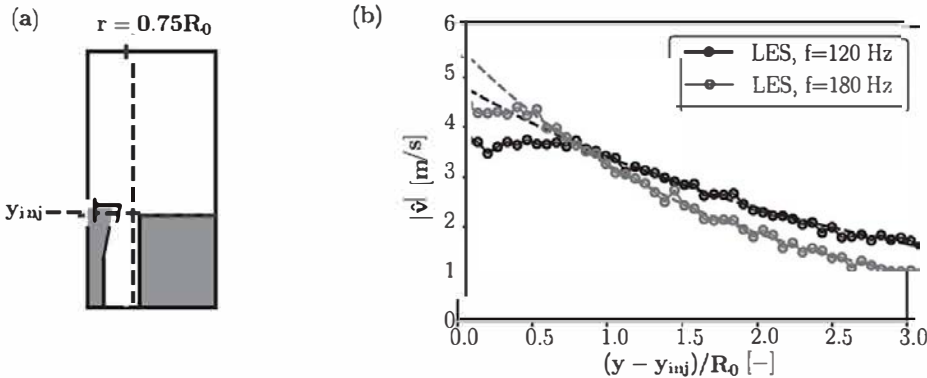


Fig. 15. (a) Schematic of the central line located at $r/R_0 = 0.75$ used for the amplitude decay evaluation. (b) Acoustic velocity amplitudes on the same line, starting from the injector exit plane. Dotted lines show the best fit for each frequency in the form $Ae^{-\gamma y}$.

ponent addition. The method is therefore iterated once gain, yielding $\chi = -0.336$. This new methodology requiring a non-reactive pulsed simulation for the decay rate determination is here denoted as SFTF3, and results are shown in Fig. 16. By stepping up to SFTF3, the FTF gain for frequencies $f \geq 150$ Hz matches reference data due to the fact that the spatial/high frequency velocity perturbation decay is taken into account. The phase curve in Fig. 16 is on the other hand only marginally modified compared to the results from SFTF2 shown in Fig. 14. From these observations, it is concluded that the SFTF strategy constitutes a modular analytical FTF model for swirled V-flames featuring different accuracy levels depending on the number of simulations the user can afford. In any case, it remains less computationally intensive than performing several single frequency forced simulations as usually needed

to reconstruct the whole FTF. Compared to a reconstruction based on system identification techniques [18,64], the method developed in this work is not restricted to vanishingly small perturbation levels and can be used to determine the frequency response of premixed swirled flames submitted to flow rate modulations of any finite arbitrary amplitude. It is recalled that the results were obtained here for a fixed perturbation RMS level $\bar{v}/\bar{v} = 0.30$.

All input parameters for the SFTF model determined using methodologies SFTF1, SFTF2 and SFTF3 are summarized in Table 4 for the sake of completeness, while a brief summary of each methodology ability to represent the flame response is available in Table 5.

From these results, and depending on the available computational resources, one can choose whether a single simulation is

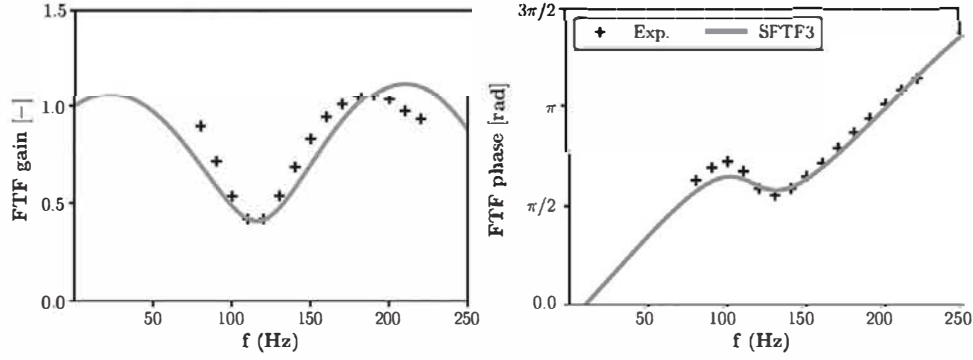


Fig. 16. SFTF3 model results with parameters estimated from a stationary LES (SFTF2), and two additional forced LES at $f = 120$ Hz for both reactive and non reactive conditions: $\omega_s/\omega = 2.43$ ms, $\alpha = 34.8^\circ$, $K = 1.36 + 0.25i$, $\chi = -0.336$, $\tau = 5.55$ ms, $\phi_0 = -0.905$ rad.

Table 4

SFTF parameters as determined from (a) a single reacting stationary LES or (b) using pointwise optimization on an additional reactive pulsed LES at $f = 120$ Hz and (c) with two additional cold/reactive pulsed LES at $f = 120$ Hz.

Case	ω_s/ω [ms]	α [deg]	K	χ	τ [ms]	ϕ_0 [rad]
(a) SFTF1	2.43	34.8	1.36	-0.33	5.55	0.0
(b) SFTF2	2.43	34.8	1.36	-0.368	5.55	-0.905
(c) SFTF3	2.43	34.8	$1.36 + 0.250i$	-0.336	5.55	-0.905

Table 5

Overview of the FTF reproduction accuracy using an increasingly complex evaluation of SFTF model parameters.

Case	nb. of LES	Agreement on gain	Agreement on phase
(a) SFTF1	1	moderate	moderate
(b) SFTF2	3	moderate	good
(c) SFTF3	4	good	good

sufficient (SFTF1), or if accuracy is sought, if it is preferable to run additional forced simulations to obtain a better representation of the FTF gain and phase (SFTF2 and SFTF3). Assessing the spatial decay rates of velocity disturbances, SFTF3, yields a complete description of the flame acoustic response at the cost of an additional non reactive pulsed simulation at any frequency compared to SFTF3.

5.4. Effect of the perturbation amplitude

All analyses performed up to this point have been made for a fixed RMS perturbation level $\hat{v}/\bar{v} = 30\%$. It is well known that while the flame acoustic response remains unchanged for low amplitude perturbations, for greater amplitudes, nonlinear interactions modify the FTF gain and phase [6,15,17,20,22]. In the particular case of fully premixed swirled flames, studies [15,48] show that increasing the forcing amplitude barely affects the position of the gain extrema of the FTF, but regularly reduces the gain for frequencies higher than the one associated to the first local gain minimum. The FTF phase lag remains unaltered by the forcing level. When it comes to the SFTF model, this implies that the time delay τ , but also the phase ϕ_0 controlling the position of this local minimum do not change when increasing the forcing level. The two remaining parameters which can therefore potentially account for effects of non-linearities are β and χ . Note also that the SFTF model itself was derived from linear acoustics theory and should therefore not be suitable for high forcing levels. Despite this theoretical limit, the model parameters are here determined from LES, which is intrinsically a nonlinear flow solver. It is therefore interesting to gauge the model ability to handle different forcing amplitudes. In order to validate the aforementioned assumptions, two additional non reacting pulsed simulations are run with RMS forcing levels

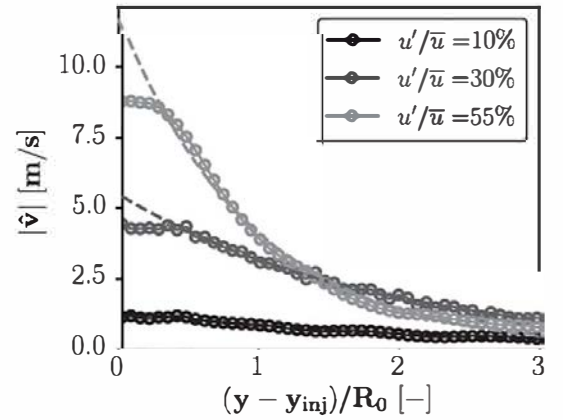


Fig. 17. Acoustic velocity amplitude at $r/R_0 = 0.75$, starting from the injector exit plane for RMS forcing levels 10%, 30% and 55% and forcing frequency $f = 180$ Hz. Dotted lines show the best fit for each amplitude in the form $Ae^{-\beta y}$.

Table 6

SFTF parameters as determined from SFTF3 procedure using $f = 180$ Hz as a target for forcing levels $\hat{v}/\bar{v} = 10\%$, 30% and 55%.

Case	ω_s/ω [ms]	α [deg]	K	χ	τ [ms]	ϕ_0 [rad]
$\hat{v}/\bar{v} = 10\%$	2.43	34.8	$1.36 + 0.20i$	-0.341	5.55	-0.905
$\hat{v}/\bar{v} = 30\%$	2.43	34.8	$1.36 + 0.26i$	-0.331	5.55	-0.905
$\hat{v}/\bar{v} = 50\%$	2.43	34.8	$1.36 + 0.50i$	-0.346	5.55	-0.905

$\hat{v}/\bar{v} = 10\%$ and $\hat{v}/\bar{v} = 55\%$. For the latter, experiments have shown a drop of the FTF gain from 1.05 for a 30% forcing level to 0.80 for a 55% forcing level at $f = 180$ Hz. The procedure described in Section 5.3 for the determination of the decay rate β is applied once again for the two new forcing levels using phase averaged data, yielding the decay curves shown in Fig. 17 obtained for $f = 180$ Hz. This frequency was chosen as it corresponds to a local FTF gain maximum. The corresponding decay rates are $\beta = 0.148$ for 10%, $\beta = 0.188$ for 30% and $\beta = 0.37$ for 55% forcing amplitude, indicating that higher dissipation occurs when increasing the perturbation strength. For each new set of parameters, χ is again deduced from an optimization using LES obtained gain and phase values for $f = 180$ Hz. Newly obtained values for χ do not differ significantly when the forcing level is varied from 10% to 55%. Note also that for $\hat{v}/\bar{v} = 30\%$, $\chi = -0.331$ is obtained for an optimization applied at $f = 180$ Hz, resulting in a coefficient very close to $\chi = -0.336$ obtained for $f = 120$ Hz in Section 5.2. Final parameters for the three considered cases are summarized in Table 6.

Resulting FTF gain and phase curves for 10% and 55% forcing levels are shown in Fig. 18.

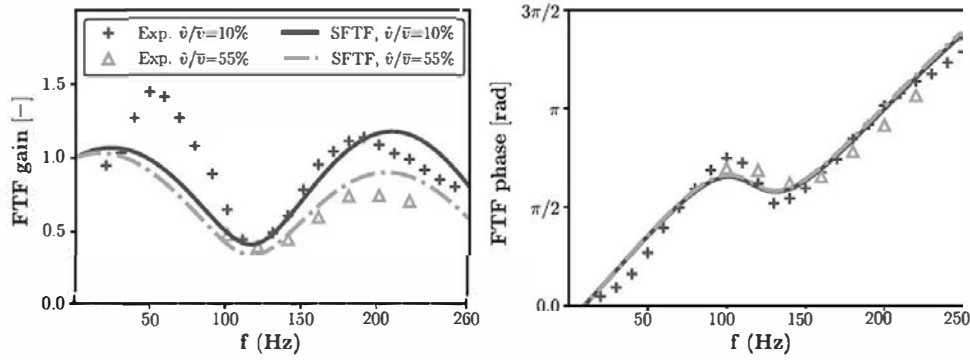


Fig. 18. SFTF3 model results for $\hat{v}/\bar{v} = 10\%$ and 55% with parameters from Table 6 and corresponding to experimental data for each forcing level.

Provided results illustrate nonlinear effects that produce a decrease of the FTF gain for high frequencies, which is indeed captured through the increase of the decay rate β . The model however fails at predicting the initial high FTF gain around $f = 60$ Hz for $\hat{v}/\bar{v} = 10\%$. Concerning the FTF phase, it is almost unaffected by the forcing amplitude. This behavior is also observed for the SFTF model, which reproduces the experimental phase quite well regardless of the forcing level.

6. Conclusion

An analytical model for the acoustic response of a premixed swirled V-shaped flame, called SFTF, has been derived as an extension of the swirling FTF model proposed by Palies et al. in [28]. The exponential decay of acoustic velocity perturbations seen in experiments is taken into account by adding a complex valued correction factor to the mean flow velocity, and the expected unity FTF gain in the low frequency limit is met thanks to a proper constraint on the model parameters. It is shown that the FTF can be characterized by a set of six distinct parameters, half of them representing the standard V-shaped flame response while the other half aims at providing the effect of swirl. By performing high fidelity simulations of a laboratory scale premixed swirled burner, it is shown that apart from experiments, LES is a good candidate for the determination of these parameters. A methodology to assess model parameters is then proposed. In this view, the final SFTF model can reach three accuracy levels SFTF1, SFTF2, SFTF3, depending on the way parameters are assessed and on the available computational resources. The design of these models can be abstracted as follows

- A first LES of the stationary flame is performed. Geometric quantities are extracted and parameters ω_*/ω , α and K , τ are appraised. The first accuracy level SFTF1 is reached.
- A pulsed LES is performed over a few periods to evaluate the phase difference ϕ_0 between the phase lag of azimuthal and axial velocity disturbances at the exit edge of the burner where large vortical structures are created and the phase lag between azimuthal and axial velocities averaged over the burner cross section area. The frequency of the first local gain minimum f_1 is then assessed from Eq. (22).
- Another pulsed LES is performed at frequency f_1 , the FTF gain and phase are evaluated at this particular frequency.
- The swirl amplitude parameter χ is obtained from a pointwise optimization process using LES estimated FTF gain and phase at f_1 . The second accuracy level SFTF2 is reached.
- An additional cold pulsed LES at any frequency is performed and the velocity disturbances decay rate β is assessed. The final fidelity level SFTF3 is finally attained, yielding quantitative results for both FTF gain and phase compared to measurements.

Model predictions are compared to FTF data determined from experiments, exhibiting characteristic swirling V-shaped flame features such as local low and high gain regions at specific frequency values, and a quasi-linear phase with undulations. Using a single stationary LES flame, the SFTF model is able to qualitatively retrieve these features and provides a first estimation of the flame response. It is then shown that using an additional reactive pulsed LES improves the model agreement with experiments by allowing to precisely evaluate the frequency of the first local FTF gain minimum. In particular, the phase evolution is already very well reproduced by the model. Finally, quantitative agreement on both FTF gain and phase is achieved with an additional cold flow pulsed simulation. Regardless of the chosen fidelity level, one reduces the global computational cost needed to compute the flame response over a broad frequency range, which would normally require several high fidelity simulations. In addition, the method works for any finite amplitude forcing and is not limited to vanishingly small perturbations. While the model is shown to perform well on this case, further investigation is needed for the evaluation of the swirl strength parameter χ which has been presently assessed by performing a pointwise optimization. Conclusions raised in this paper will be confronted to other V-shaped flame configurations to further validate the model and methodology, with varying swirler-chamber distances or differently shaped bluff bodies for instance.

Declaration of Competing Interest

The authors declare that they have no known competing financial interests or personal relationships that could have appeared to influence the work reported in this paper.

Acknowledgments

The authors gratefully acknowledge the financial support from Safran Aircraft Engines for this research. This project has received funding from the European Union's Horizon 2020 research and innovation programme under the Marie Skłodowska-Curie grant agreement No 643134. This work was granted access to the HPC resources of CINES (MESR, Montpellier, France) under allocation A0052B10157 made by GENCI on supercomputers OCCIGEN and IRENE.

Supplementary material

Supplementary material associated with this article can be found, in the online version, at doi:10.1016/j.combustflame.2020.03.026.

References

- [1] T.C. Lieuwen, V. Yang, *Combustion Instabilities in Gas Turbines Engines, Operational Experience, Fundamental Mechanisms, and Modeling*, American Institute of Aeronautics and Astronautics, 2005.
- [2] L.Y. Gicquel, G. Staffelbach, T. Poinso, Large eddy simulations of gaseous flames in gas turbine combustion chambers, *Progr. Energy Combust. Sci.* 38 (6) (2012) 782–817.
- [3] T. Poinso, Prediction and control of combustion instabilities in real engines, *Proc. Combust. Inst.* 36 (1) (2017) 1–28.
- [4] S. Candel, Combustion dynamics and control: progress and challenges, *Proc. Combust. Inst.* 29 (1) (2002) 1–28.
- [5] A. Dowling, A kinematic model of a ducted flame, *J. Fluid Mech.* 394 (1999) 51–72.
- [6] N. Noiray, D. Durox, T. Schuller, S. Candel, A unified framework for nonlinear combustion instability analysis based on the flame describing function, *J. Fluid Mech.* 615 (2008) 139–167.
- [7] A.P. Dowling, S.R. Stow, Acoustic analysis of gas turbine combustors, *J. Propuls. Power* 19 (5) (2003) 751–764.
- [8] T. Sattelmayer, W. Polifke, Assessment of methods for the computation of linear stability of combustors, *Combust. Sci. Technol.* 175 (3) (2003) 453–476.
- [9] F. Nicoud, L. Benoit, C. Sensiau, T. Poinso, Acoustic modes in combustors with complex impedances and multidimensional active flames, *AIAA J.* 45 (2) (2007) 426–441.
- [10] S. Camporeale, B. Fortunato, G. Campa, A finite element method for three-dimensional analysis of thermo-acoustic combustion instability, *J. Eng. Gas Turbines Power* 133 (1) (2011) 011506.
- [11] C.F. Silva, F. Nicoud, T. Schuller, D. Durox, S. Candel, Combining a Helmholtz solver with the flame describing function to assess combustion instability in a premixed swirled combustor, *Combust. Flame* 160 (9) (2013) 1743–1754.
- [12] X. Han, J. Li, A.S. Morgans, Prediction of combustion instability limit cycle oscillations by combining flame describing function simulations with a thermoacoustic network model, *Combust. Flame* 162 (10) (2015) 3632–3647.
- [13] F. Ni, M. Miguel-Brebion, F. Nicoud, T. Poinso, Accounting for acoustic damping in a Helmholtz solver, *AIAA J.* (2016) 1205–1220.
- [14] D. Laera, T. Schuller, K. Prieur, D. Durox, S.M. Camporeale, S. Candel, Flame describing function analysis of spinning and standing modes in an annular combustor and comparison with experiments, *Combust. Flame* 184 (2017) 136–152.
- [15] P. Palies, D. Durox, T. Schuller, S. Candel, The combined dynamics of swirler and turbulent premixed swirling flames, *Combust. Flame* 157 (9) (2010) 1698–1717.
- [16] K. Kim, J. Lee, H. Lee, B. Quay, D. Santavica, Characterization of forced flame response of swirl-stabilized turbulent lean-premixed flames in a gas turbine combustor, *J. Eng. Gas Turbines Power* 132 (041502) (2010).
- [17] B. Cosic, S. Terhaar, J. Moeck, C. Paschereit, Response of a swirl-stabilized flame to simultaneous perturbations in equivalence ratio and velocity at high oscillation amplitudes, *Combust. Flame* 162 (2015) 1046–1062.
- [18] L.T.W. Chong, T. Komarek, R. Kaess, S. Foller, W. Polifke, Identification of flame transfer functions from LES of a premixed swirl burner, *GT2010-22769*, Proceedings of the ASME Turbo Expo, American Society of Mechanical Engineers (2010), pp. 623–635.
- [19] S. Wysocki, G. Di-Chiaro, F. Biagioli, Effect of fuel mixture fraction and velocity perturbations on the flame transfer function of swirl stabilized flames, *Combust. Theory Model.* 19 (6) (2015) 714–743.
- [20] X. Han, A.S. Morgans, Simulation of the flame describing function of a turbulent premixed flame using an open-source LES solver, *Combust. Flame* 162 (5) (2015) 1778–1792.
- [21] A. Chatelier, T. Guiberti, R. Mercier, N. Bertier, B. Fiorina, T. Schuller, Experimental and numerical investigation of the response of a swirled flame to flow modulations in a non-adiabatic combustor, *Flow Turbul. Combust.* 102 (4) (2019) 995–1023.
- [22] D. Pampaloni, A. Andreini, B. Facchini, C. Paschereit, Large-eddy-simulation modeling of the flame describing function of a lean-premixed swirl-stabilized flame, *J. Propuls. Power* 35 (5) (2019) 994–1004.
- [23] D. You, Y. Huang, V. Yang, A generalized model of acoustic response of turbulent premixed flame and its application to gas-turbine combustion instability analysis, *Combust. Sci. Technol.* 177 (5–6) (2005) 1109–1150.
- [24] O.S. Graham, A. Dowling, A low-order modelling of ducted flames with temporally varying equivalence ratio in realistic geometries, *GT2011-45255*, Proceedings of the ASME Turbo Expo, 2011.
- [25] B. Semlitsch, A. Orchini, A.P. Dowling, M.P. Juniper, G-equation modelling of thermoacoustic oscillations of partially premixed flames, *Int. J. Spray Combust. Dyn.* 9 (4) (2017) 260–276.
- [26] T. Komarek, W. Polifke, Impact of swirl fluctuations on the flame response of a perfectly premixed swirl burner, *J. Eng. Gas Turbines Power* 132 (6) (2010) 061503.
- [27] K.T. Kim, D.A. Santavica, Interference mechanisms of acoustic/convective disturbances in a swirl-stabilized lean-premixed combustor, *Combust. Flame* 160 (8) (2013) 1441–1457.
- [28] P. Palies, T. Schuller, D. Durox, S. Candel, Modeling of premixed swirling flames transfer functions, *Proc. Combust. Inst.* 33 (2) (2011a) 2967–2974.
- [29] P. Palies, D. Durox, T. Schuller, S. Candel, Acoustic-convective mode conversion in an aerofoil cascade, *J. Fluid Mech.* 672 (2011b) 545–569.
- [30] T. Schuller, D. Durox, S. Candel, A unified model for the prediction of laminar flame transfer functions: comparisons between conical and V-flame dynamics, *Combust. Flame* 134 (1) (2003) 21–34.
- [31] L. Tay-Wo-Chong, S. Bomberg, A. Ulhaq, T. Komarek, W. Polifke, Comparative validation study on identification of premixed flame transfer function, *J. Eng. Gas Turbines Power* 134 (2) (2012) 021502.
- [32] M. Fleifil, A.M. Annaswamy, Z. Ghoneim, A.F. Ghoniem, Response of a laminar premixed flame to flow oscillations: a kinematic model and thermoacoustic instability results, *Combust. Flame* 106 (4) (1996) 487–510.
- [33] R. Balachandran, B. Ayoola, C. Kaminski, A. Dowling, E. Mastorakos, Experimental investigation of the nonlinear response of turbulent premixed flames to imposed inlet velocity oscillations, *Combust. Flame* 143 (1–2) (2005) 37–55.
- [34] T. Steinbacher, A. Albayrak, A. Ghani, W. Polifke, Consequences of flame geometry for the acoustic response of premixed flames, *Combust. Flame* 199 (2019) 411–428.
- [35] Preetham, H. Santosh, T. Lieuwen, Dynamics of laminar premixed flames forced by harmonic velocity disturbances, *J. Propuls. Power* 24 (6) (2008) 1390–1402.
- [36] D. Durox, T. Schuller, S. Candel, Combustion dynamics of inverted conical flames, *Proc. Combust. Inst.* 30 (2) (2005) 1717–1724.
- [37] D. Durox, T. Schuller, N. Noiray, S. Candel, Experimental analysis of nonlinear flame transfer functions for different flame geometries, *Proc. Combust. Inst.* 32 (1) (2009) 1391–1398.
- [38] T. Schuller, S. Ducruix, D. Durox, S. Candel, Modeling tools for the prediction of premixed flame transfer functions, *Proc. Combust. Inst.* 29 (1) (2002) 107–113.
- [39] A.-L. Birbaud, D. Durox, S. Candel, Upstream flow dynamics of a laminar premixed conical flame submitted to acoustic modulations, *Combust. Flame* 146 (3) (2006) 541–552.
- [40] A. Cuquel, Dynamics and nonlinear thermo-acoustic stability analysis of premixed conical flames, Châtenay-Malabry, Ecole centrale de Paris, 2013 Ph.D. thesis.
- [41] Z. Han, S. Hochgreb, The response of stratified swirling flames to acoustic forcing: experiments and comparison to model, *Proc. Combust. Inst.* 35 (3) (2015) 3309–3315.
- [42] W. Polifke, C. Lawn, On the low-frequency limit of flame transfer functions, *Combust. Flame* 151 (3) (2007) 437–451.
- [43] M. Merk, W. Polifke, R. Gaudron, M. Gatti, C. Mirat, T. Schuller, Measurement and simulation of combustion noise and dynamics of a confined swirl flame, *AIAA J.* 56 (2018) 1930–1942.
- [44] M. Merk, C. Silva, W. Polifke, M. Gaudron, R. Gatti, C. Mirat, T. Schuller, Direct assessment of the acoustic scattering matrix of a turbulent swirl combustor by combining system identification, large eddy simulation and analytical approaches, *J. Gas Turbines Power* 141 (21035) (2019).
- [45] M. Merk, R. Gaudron, M. Gatti, C. Mirat, W. Polifke, T. Schuller, Quantitative comparisons between LES predictions and experimental measurements of sound pressure spectra in a confined swirl combustor, *53rd AIAA/SAE/ASME Joint Propulsion Conference* (2017), p. 4687.
- [46] M. Gatti, R. Gaudron, C. Mirat, L. Zimmer, T. Schuller, Impact of swirl and bluff-body on the transfer function of premixed flames, *Proc. Combust. Inst.* 37 (2019) 5197–5204.
- [47] M. Gatti, R. Gaudron, C. Mirat, L. Zimmer, T. Schuller, A comparison of the transfer functions and flow fields of flames with increasing swirl number, *GT2018-76105*, Proceedings of the ASME Turbo Expo, 2018.
- [48] M. Gatti, Combustion dynamics of premixed swirling flames with different injection conditions, 2019 Ph.D. thesis.
- [49] O. Colin, M. Rudgyard, Development of high-order Taylor–Galerkin schemes for LES, *J. Comput. Phys.* 162 (2) (2000) 338–371.
- [50] T.J. Poinso, S. Lele, Boundary conditions for direct simulations of compressible viscous flows, *J. Comput. Phys.* 101 (1) (1992) 104–129.
- [51] F. Nicoud, H.B. Toda, O. Cabrit, S. Bose, J. Lee, Using singular values to build a subgrid-scale model for large eddy simulations, *Phys. Fluids* 23 (8) (2011) 085106.
- [52] O. Colin, F. Ducros, D. Veynante, T. Poinso, A thickened flame model for large eddy simulations of turbulent premixed combustion, *Phys. Fluids* 12 (7) (2000) 1843–1863.
- [53] B. Franzelli, E. Riber, L.Y. Gicquel, T. Poinso, Large eddy simulation of combustion instabilities in a lean partially premixed swirled flame, *Combust. Flame* 159 (2) (2012) 621–637.
- [54] G. Daviller, M. Brebion, P. Xavier, G. Staffelbach, J.-D. Müller, T. Poinso, A mesh adaptation strategy to predict pressure losses in LES of swirled flows, *Flow Turbul. Combust.* 99 (1) (2017) 93–118.
- [55] J. Herrin, J. Dutton, An investigation of Idiv velocity bias correction techniques for high-speed separated flows, *Exp. Fluids* 15 (4–5) (1993) 354–363.
- [56] R. Mercier, T. Guiberti, A. Chatelier, D. Durox, O. Gicquel, N. Darabiha, T. Schuller, B. Fiorina, Experimental and numerical investigation of the influence of thermal boundary conditions on premixed swirling flame stabilization, *Combust. Flame* 171 (2016) 42–58.
- [57] C. Kraus, L. Selle, T. Poinso, Coupling heat transfer and large eddy simulation for combustion instability prediction in a swirl burner, *Combust. Flame* 191 (2018) 239–251.
- [58] D. Kim, J.G. Lee, B.D. Quay, D. Santavica, K. Kim, S. Srinivasan, Effect of flame structure on the flame transfer function in a premixed gas turbine combustor, *J. Eng. Gas Turbine Power* 132 (021502) (2010).
- [59] T. Günther, H. Theisel, The state of the art in vortex extraction, *Computer Graphics Forum*, 37, Wiley Online Library (2018), pp. 149–173.

- [60] U. Rist, Visualization and tracking of vortices and shear layers in the late stages of boundary-layer laminar-turbulent transition, AIAA2012-008 50th AIAA Aerospace Sciences Meeting including the New Horizons Forum and Aerospace Exposition (2012), p. 84.
- [61] P. Palies, D. Durox, T. Schuller, S. Candel, Experimental study on the effect of swirler geometry and swirl number on flame describing functions, *Combust. Sci. Technol.* 183 (7) (2011) 704–717.
- [62] A. Albayrak, M.P. Juniper, W. Polifke, Propagation speed of inertial waves in cylindrical swirling flows, *J. Fluid Mech.* 879 (2019) 85–120.
- [63] L. Selle, F. Nicoud, T. Poinso, Actual impedance of nonreflecting boundary conditions: implications for computation of resonators, *AIAA J.* 42 (5) (2004) 958–964.
- [64] W. Polifke, Black-box system identification for reduced order model construction, *Ann. Nucl. Energy* 67 (2014) 109–128.
- [65] P. Palies, T. Schuller, D. Durox, L. Gicquel, S. Candel, Acoustically perturbed turbulent premixed swirling flames, *Phys. Fluids* 23 (3) (2011) 037101.